The COSMO model: towards cloud-resolving NWP

Michael Baldauf

Deutscher Wetterdienst
Frankfurter Str. 135
63067 Offenbach
Germany

1   Introduction

At the Deutscher Wetterdienst (DWD) the COSMO model is currently used in two different settings: the COSMO-EU with a grid mesh size of about 7 km covers most of the European continent and is driven by the global model GME. Nested into COSMO-EU is the convection-permitting model COSMO-DE with a grid mesh size of about 2.8 km. Similar setups are also used by most of the COSMO partners (Greece, Italy, Poland, Russia, Romania, Switzerland). DWD additionally uses COSMO-DE in an ensemble system with 20 members. At the end of 2014, GME will be replaced by the newly developed global model ICON (see the article by G. Zängl in these proceedings). Probably mid of 2015, COSMO-EU will be replaced by the static grid-refinement possibility of ICON, too.

The current COSMO model uses the so called 'Runge-Kutta' dynamical core; a few aspects of that are addressed in sections 2 and 3. In particular, section 2 highlights consequences from the staggering in a vertically stretched grid.

One drawback of the current dynamical core is its non-conservation of all prognostic variables. Therefore, during the years 2008-2012, the COSMO priority project 'Conservative Dynamical Core (CDC)' (Baldauf *et al.*, 2013a) investigated two other possible candidates, namely the dynamical core of the EULAG model (e.g. Prusa *et al.* (2008)) and a fully implicit finite volume solver (Jameson, 1991). Additionally, in the framework of the German Research Foundation program 'Metström', the Discontinuous Galerkin (DG) method is investigated for meteorological applications. This and the above mentioned two dynamical cores of the CDC project are formulated on an unstaggered grid. Consequently, the last section 4 investigates the properties of wave expansion in the DG formulation on unstaggered grids.

2   The new fast waves solver of the COSMO model - consequences from the vertically stretched grid

2.1   A new fast waves solver

The basic time integration scheme of the COSMO model is quite similar to that of the WRF model (Wicker and Skamarock, 2002; Baldauf, 2010): it is a split-explicit scheme which uses a large time step for the 'slow' processes advection, Coriolis force and the physical tendencies and a small time step for the 'fast waves' (sound and gravity waves). This time-splitting procedure is embedded into a 3-stage Runge-Kutta scheme, which stably integrates the 5th order advection until Courant numbers of 1.42 (Baldauf, 2008). For the fast processes 2nd order centred differences for the spatial discretisation and a horizontally forward-backward, vertically implicit (HE-VI) time integration is used.

During the last about two years a new fast waves solver has been developed (Baldauf, 2013) which mainly improves the following items:

1. use of weighted averaging operations for *all* vertical discretisations (also the implicit ones),

2. formulation of the divergence operator in strong conservation form,

3. the option to use a fully 3-dimensional (i.e. isotropic) divergence damping (instead of applying it only to the horizontal momentum equations),

4. the option to use the Mahrer (1984) discretisation for the horizontal pressure gradient terms.

Apart from that also smaller improvements e.g. in the formulation of boundary conditions or to fulfil an additional slope-dependent stability condition for the divergence damping have been done. This new fast waves solver is contained in the official COSMO version 4.24 and is in operational use at DWD since 16 Jan. 2013. It turned out, that it improves the overall numerical stability; this has been shown in several real test cases that crashed before. In particular the ability to treat slightly steeper slopes has been improved.

2.2 Vertically stretched grids

In the following we will consider the first item in the above list, the improvement of the discretisation for vertically stretched grids. Generally the vertical stretching in the most operational applications is quite large. At DWD the COSMO model uses a grid mesh size of $\Delta z = 20$ m at the ground and $\Delta z \approx 1000$ m at the model top. This huge stretching needs of course special attention.

As an example we consider the discretisation of a first derivative $\partial \psi / \partial z$ in a stretched grid with grid points z_k. We consider only at most 3-point formulae because the tridiagonal solver in the split-explicit scheme does not allow wider stencils (solvers using more diagonals than three are possibly too inefficient for HE-VI schemes). There are in principal two ways of discretising this. The first approach uses weightings in the original space (Ikeda and Durbin, 2004), e.g.

$$\left.\frac{\partial \psi}{\partial z}\right|_{z_k} = \frac{z_{k+1} - z_k}{z_{k+1} - z_{k-1}} \cdot \frac{\psi_k - \psi_{k-1}}{z_k - z_{k-1}} + \frac{z_k - z_{k-1}}{z_{k+1} - z_{k-1}} \cdot \frac{\psi_{k+1} - \psi_k}{z_{k+1} - z_k}, \tag{1}$$

which can be derived by using a quadratic function through the three points.
In the second approach the coordinates z_k are given by a coordinate transformation $z_k = f(\zeta_k)$, $\zeta_k = k\Delta\zeta$ and the derivative can be calculated via the chain rule by

$$\left.\frac{\partial \psi}{\partial z}\right|_{z_k} = \frac{\partial \zeta}{\partial z} \left.\frac{\partial \psi}{\partial \zeta}\right|_{\zeta_k}, \tag{2}$$

where the second factor on the right is calculated e.g. by centred differences.

Both approaches are straightforward in an unstaggered A-grid but it is less clear how to proceed in a staggered C-grid (or Lorenz grid). In the COSMO model the *half* levels $z_{k+\frac{1}{2}}$ (where the vertical velocities w are located) are defined by prescribed values which are additionally stretched according to the orography elevation. Here, we can consider them as given by the above mentioned stretching function. The *main* levels z_k (position of all scalars and (horizontally staggered) of the u and v velocity components) are located exactly in the middle of two half levels

$$z_{i,j,k} = \frac{z_{i,j,k+\frac{1}{2}} + z_{i,j,k-\frac{1}{2}}}{2} \tag{3}$$

(see figure 1). Consequently, if one wants to interpolate from half levels to main levels an arithmetic average

$$\bar{\psi}_{i,j,k} = \frac{1}{2}(\psi_{i,j,k-\frac{1}{2}} + \psi_{i,j,k+\frac{1}{2}}) \tag{4}$$

is used, whereas for interpolations from main levels to half levels a weighted average

$$\bar{\psi}_{i,j,k-\frac{1}{2}} = g_{i,j,k-\frac{1}{2}}\psi_{i,j,k} + (1 - g_{i,j,k-\frac{1}{2}})\psi_{i,j,k-1} \tag{5}$$

is used now, in which the weights g take into account the grid distance. Derivatives are calculated always by centred differences, possibly after an appropriate weighting of fields, if necessary.

One may ask, why such a weighting is necessary at all and why one cannot simply use the above mentioned second approach. The answer is, that in this special staggering, i.e. the asymmetry in the definition of main and half levels, not every information is contained in the metric coefficients (as would be the case in an unstaggered grid). Due to this delicate asymmetry, we need a tool to decide which discretisation is the best in stretched grids. As such a tool we use a truncation error analysis. This is a straightforward task for an equidistant grid, because one can simply led the grid mesh size $\Delta z \to 0$. However, for non-equidistant grids there exist infinitely many possibilities to refine a grid. In the following, two variants of grid refinements are analysed, that lead to different orders of the truncation error.
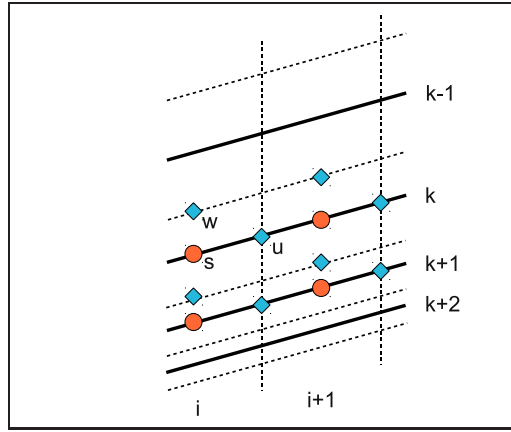

Figure 1: Grid positions and stretching in COSMO.

Discretisation error analysis - variant A In the first variant, the grid stretching is described by the above mentioned *coordinate transformation* $z_{k+\frac{1}{2}} = z(\zeta_{k+\frac{1}{2}})$. The transformed coordinate ζ generates an equidistant grid $\zeta_{k+\frac{1}{2}} = (k+1/2) \cdot \Delta\zeta$. With increasing grid refinement $\Delta\zeta \to 0$ all the grid mesh sizes $\Delta z_k := z_{k-\frac{1}{2}} - z_{k+\frac{1}{2}} \approx \frac{\partial z}{\partial \zeta}\big|_k \cdot \Delta\zeta$ converge to 0, too. Hence, the convergence inspection takes place for $\Delta\zeta \to 0$.

With decreasing $\Delta\zeta$ the stretching function *locally* becomes increasingly linear. Consequently, with this approach to refine the grid one gets formally 2nd order truncation errors for all two-point discretisations.

Discretisation error analysis - variant B To avoid the circumstance, that for increasing resolution $\Delta z_k \to 0$ the grid stretching becomes *locally* more and more linear, one can prescribe a constant grid stretching

$$\frac{\Delta z_k}{\Delta z_{k-1}} = s$$

instead. Without any loss of generality we can assume that $s > 1$, i.e. the grid becomes finer in the vicinity of $z_0 = 0$. To this purpose we choose the grid points in

$$\ldots, \quad z_{i,-1-\frac{1}{2}}^{(h)} = h(x_i) - \frac{1}{2}\Delta z - \frac{1}{s}\Delta z, \quad z_{i,-\frac{1}{2}}^{(h)} = h(x_i) - \frac{1}{2}\Delta z,$$
$$z_{i,\frac{1}{2}}^{(h)} = h(x_i) + \frac{1}{2}\Delta z, \quad z_{i,1+\frac{1}{2}}^{(h)} = h(x_i) + \frac{1}{2}\Delta z + s\Delta z, \quad \ldots. \tag{6}$$

Here the prescription of a slope by $h(x)$ is possible. The flattening of coordinate surfaces with increasing height is neglected. The position of the main levels again is defined by Eq. (3).

One has to note, that such a grid refinement does not converge *globally*, because one inserts smaller and smaller grid boxes only on one end of the interval (at $z = 0$), without a significant refinement at the other end (Baldauf, 2013).

2.2.1 Buoyancy term in the w-equation

Now we perform Taylor expansions for $\Delta x \to 0$ and $\Delta \zeta \to 0$ *around the position of the target point* (which itself can be a function of Δx and $\Delta \zeta$, too). At first, terms of the form T'/T_0 (or analogously p'/p) occurring in the buoyancy term of the w-equation are inspected.

Discretisation error analysis - variant A. With the above mentioned weighted vertical interpolations for T' (and the exact value of a reference temperature T_0 at the w-position) one gets

$$\overline{\frac{T'}{T_0}} = \frac{T'}{T_0} + \Delta \zeta^2 \frac{1}{T_0} \left[\frac{1}{8} \left(\frac{\partial z}{\partial \zeta} \right)^2 \frac{\partial^2 T'}{\partial z^2} \right] + O(\Delta \zeta^4). \tag{7}$$

Whereas with the simple arithmetic average it follows

$$\overline{\frac{T'}{T_0}} = \frac{T'}{T_0} + \Delta \zeta^2 \frac{1}{T_0} \left[\frac{1}{8} \left(\frac{\partial z}{\partial \zeta} \right)^2 \frac{\partial^2 T'}{\partial z^2} + \frac{1}{4} \frac{\partial^2 z}{\partial \zeta^2} \frac{\partial T'}{\partial z} \right] + O(\Delta \zeta^4). \tag{8}$$

Compared to the weighted version an additional term occurs, which stems from the curvature of the coordinate transformation. Since no statements about the sign of these terms can be done, it is at this point hard to say which discretisation is the better one. However, the following analysis of the grid stretching variant B gives a clearer statement.

Discretisation error analysis - variant B. Now we use a grid analogous[1] to (6).

Use of weighted vertical interpolations for T' results in

$$\overline{\frac{T'}{T_0}} = \frac{T'}{T_0} + \Delta z \cdot 0 + \Delta z^2 \left[\frac{1}{2} \frac{s}{(s+1)^2} \frac{1}{T_0} \frac{\partial^2 T'}{\partial z^2} \right] + O(\Delta z^3). \tag{9}$$

Through the weighting this discretisation is indeed of 2nd order in Δz.

Simple arithmetic average in the vertical results in

$$\overline{\frac{T'}{T_0}} = \frac{T'}{T_0} + \Delta z \left[\frac{1}{2} \frac{s-1}{s+1} \frac{1}{T_0} \frac{\partial T'}{\partial z} \right] + \Delta z^2 \left[\frac{1}{4} \frac{s^2+1}{(s+1)^2} \frac{1}{T_0} \frac{\partial^2 T'}{\partial z^2} \right] + O(\Delta z^3). \tag{10}$$

This is only of first order for all $s \neq 1$.

Now, the advantage of using weighted interpolations is obvious.

---

[1] Actually, a slightly different grid is used, because this leads to more symmetric formulae in s if applied to the w equation terms, see Baldauf (2013).

2.2.2 The divergence term

The same analysis is done now for the 2-dimensional divergence operator in terrain-following coordinates

$$\operatorname{div}\mathbf{v} = \frac{1}{\sqrt{g}}\left[\frac{\partial\sqrt{g}u(x,\zeta)}{\partial x} + \frac{\partial}{\partial\zeta}\left(\frac{\partial z}{\partial x}u - w\right)\right] \qquad (11)$$

Here, the metric term $\frac{\partial}{\partial\zeta}\frac{\partial z}{\partial x}u$ requires a weighted interpolation of u to the half level position.

Discretisation error analysis - variant A. Interpolation by a weighted vertical average delivers

$$
\begin{aligned}
\operatorname{div}\mathbf{v} =\ & \frac{\partial u(x,z)}{\partial x} + \frac{\partial w(x,z)}{\partial z} + \Delta\zeta^2\left(-\frac{1}{4}\frac{\partial^2 z}{\partial x\partial\zeta}\frac{\partial z}{\partial\zeta}\frac{\partial^2 u}{\partial z^2} - \frac{1}{4}\frac{\partial^2 z}{\partial\zeta^2}\frac{\partial z}{\partial x}\frac{\partial^2 u}{\partial z^2}\right.\\
& \left. - \frac{1}{6}\left(\frac{\partial z}{\partial\zeta}\right)^2\frac{\partial z}{\partial x}\frac{\partial^3 u}{\partial z^3} + \frac{1}{24}\left(\frac{\partial z}{\partial\zeta}\right)^2\frac{\partial^3 w}{\partial z^3}\right) + \Delta x^2(\ldots) + \ldots
\end{aligned}
\qquad (12)
$$

whereas with only arithmetic averaging the second term in brackets has a twice as large coefficient and two additional terms occur:

$$
\begin{aligned}
\operatorname{div}\mathbf{v} =\ & \frac{\partial u(x,z)}{\partial x} + \frac{\partial w(x,z)}{\partial z} + \Delta\zeta^2\left(-\frac{1}{4}\frac{\partial^2 z}{\partial x\partial\zeta}\frac{\partial z}{\partial\zeta}\frac{\partial^2 u}{\partial z^2} - \frac{1}{2}\frac{\partial^2 z}{\partial\zeta^2}\frac{\partial z}{\partial x}\frac{\partial^2 u}{\partial z^2}\right.\\
& - \frac{1}{6}\left(\frac{\partial z}{\partial\zeta}\right)^2\frac{\partial z}{\partial x}\frac{\partial^3 u}{\partial z^3} + \frac{1}{24}\left(\frac{\partial z}{\partial\zeta}\right)^2\frac{\partial^3 w}{\partial z^3}\\
& \left. - \frac{1}{4}\frac{\partial\zeta}{\partial z}\frac{\partial^2 z}{\partial x\partial\zeta}\frac{\partial^2 z}{\partial\zeta^2}\frac{\partial u}{\partial z} - \frac{1}{4}\frac{\partial\zeta}{\partial z}\frac{\partial^3 z}{\partial\zeta^3}\frac{\partial z}{\partial x}\frac{\partial u}{\partial z}\right) + \Delta x^2(\ldots) + \ldots
\end{aligned}
\qquad (13)
$$

We see already here the benefit from the weightings.

Discretisation error analysis - variant B. Again we use the grid given by (6). If the metric term is discretised by a weighted vertical average it follows

$$\operatorname{div}\mathbf{v} = \frac{\partial u(x,z)}{\partial x} + \frac{\partial w(x,z)}{\partial z} + \Delta z\left(\frac{1}{8}\frac{\partial h}{\partial x}\frac{\partial^2 u}{\partial z^2}\left(\frac{1}{s}-s\right)\right) + O(\Delta z^2, \Delta x^2), \qquad (14)$$

whereas with a discretisation by only an arithmetic average it follows

$$
\begin{aligned}
\operatorname{div}\mathbf{v} =\ & \frac{\partial u(x,z)}{\partial x} + \frac{\partial h}{\partial x}\frac{\partial u(x,z)}{\partial z}\left(\frac{1}{2} - \frac{1}{4}\left(s + \frac{1}{s}\right)\right) + \frac{\partial w(x,z)}{\partial z} + \\
& + \Delta z\left(\frac{1}{8}\frac{\partial h}{\partial x}\frac{\partial^2 u}{\partial z^2}\left(\left(\frac{1}{s}-s\right) + \frac{1}{2}\left(\frac{1}{s^2}-s^2\right)\right)\right) + O(\Delta z^2, \Delta x^2).
\end{aligned}
\qquad (15)
$$

For a stretched grid ($s \neq 1$) *and* on a tilted coordinate this is not a consistent discretisation at all!

To summarise, the higher numerical stability of the new fast waves solver (in particular in steeper terrain) stems at least partly from a better and more consistent discretisation in a vertically stretched grid. Proper derivation (use of the exact positions of half and main levels!) of truncation errors helps in the decision in which way weightings should be used.

2.3 Comparison with an exact analytical solution

To check the previous theoretical considerations and to prove the benefit of the weightings an idealised test with a vertically stretched grid is performed (see also Baldauf (2013)).

The test uses the expansion of quasi-linear gravity and sound waves induced by a weak warm bubble in a channel. This test setup was proposed by Skamarock and Klemp (1994). Recently, an analytic solution for the linearised, *compressible*, non-hydrostatic Euler equations and for an isothermal atmosphere has been found (Baldauf and Brdar, 2013). Because this analytical solution bases on exactly the same equation set as the COSMO model, the numerical model exactly converges to this solution, as long as non-linear terms remain small. This test case inspects almost all terms of the fast waves solver (with the exception of the 'horizontal' metric terms) together with the time integration scheme and the coupling with the advection process.

The so called 'small-scale' test setup consists of a weak warm bubble, which is set into a 10 km high and 300 km wide channel with periodic boundary conditions in the horizontal. To demonstrate the benefit of the vertical weightings in the new fast waves solver (FW2) a vertical grid stretching is introduced, with a grid stretching ratio of 1:10 between the finest vertical mesh size around $z = 5$ km and the coarsest mesh size around $z = 0$ and $z = 10$ km. Figures 2 show the grid for the first two chosen (horizontal) resolutions $\Delta x = 1000$ m and 500 m with 300×20 and 600×40 grid points, respectively, and the initial temperature perturbation T' of the weak warm bubble at $t = 0$. The time steps for these simulations are 20 s and 10 s, respectively, and analogous for the finer resolutions. During the expansion of the waves a background velocity field with $u_0 = 20$ m/s advects the waves to the right. Figure 3 shows the solution for T' and w of FW2 after 30 min. together with the analytic solution.
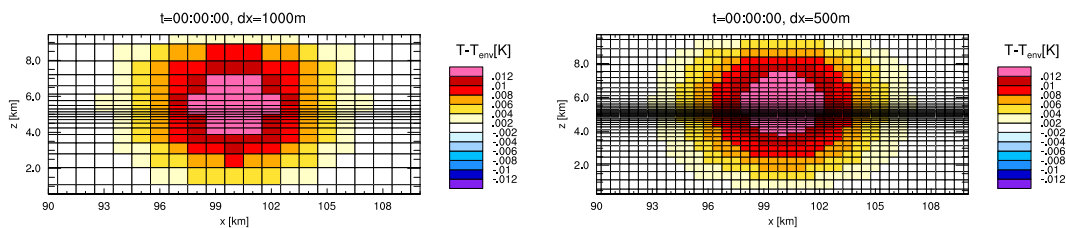

Figure 2: Grid and initial temperature perturbation $T'(t = 0)$ for the first two resolutions $\Delta x = 1000$ m, 500 m for the linear gravity/sound wave test.
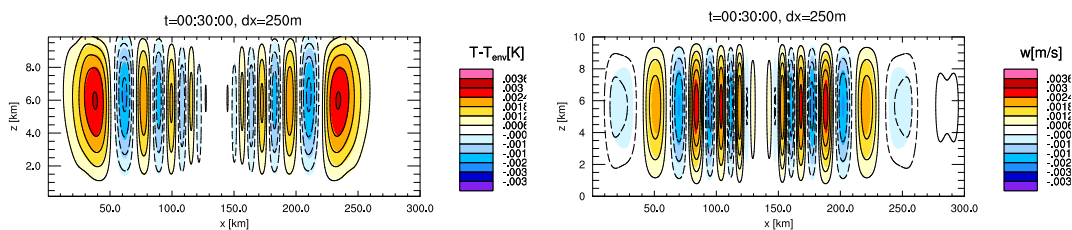

Figure 3: Temperature perturbation T' and vertical velocity w after 30 min. for $\Delta x = 250$ m horizontal resolution. Comparison between FW2-simulation (shaded) and analytic solution (lines).

Figures 4 show the error norms L_2 and L_∞ (the maximum norm) of the simulated solution against the analytic solution after 30 min. In all cases, the errors of the new fast waves solver (FW2) are smaller compared to those of the old one (FW1). For the coarsest resolution the error of FW1 is nearly twice as large compared to FW2. One should notice that the more gentle slope for FW2 does not mean a smaller convergence rate. As one can see from the curvature of the lines, the simulation for the coarser resolutions is not yet in the convergence range. In contrast, these error norms show that the errors for not completely resolved structures are better with the vertical weightings in the new FW2. For very fine resolutions the error norms of FW1 and FW2 are nearly the same and result in a convergence rate of

about 0.7 for T'. The reason for this behaviour is, that for an increasing number of vertical grid points, the local grid stretching becomes increasingly linear. This can be seen in figures 2, too. Consequently, the importance of the weightings in the averages decreases.
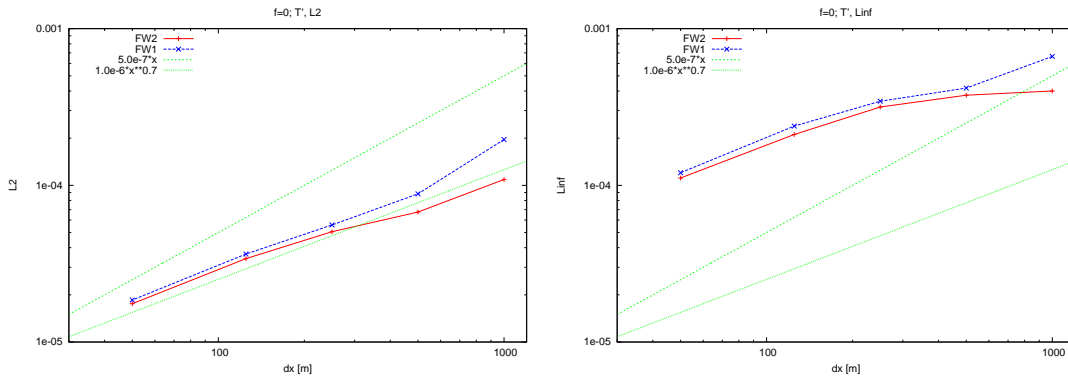

Figure 4: Linear gravity/sound wave test with vertically stretched grid. Error norms of T' against the analytic solution for the new fast waves solver (FW2, red) and the old one (FW1, blue) for different resolutions.

2.3.1 Analytic solution on the sphere

Recently an analogous analytical solution for the linearised, compressible, non-hydrostatic Euler equations *on the sphere* has been found (Baldauf *et al.*, 2013b). Here, gravity and sound waves induced by a weak warm bubble expand in a spherical shell around the sphere (instead of a horizontal channel). Figure 5 show L_2 and L_∞ errors of T' and w for the ICON model against this solution for 'test scenario (B)', i.e. with Coriolis force in the 'global f-plane approximation'. On the left, sound waves are slightly damped by a weak off-centring in the vertical and by an extrapolation by the timelevel $n-1$ in the horizontal pressure gradient. This results in a first order convergence of ICON. On the right, these damping mechanisms are switched off (the ICON model nevertheless remains stable, as long as all physical parameterisations are switched off); this results in the expected second order convergence.
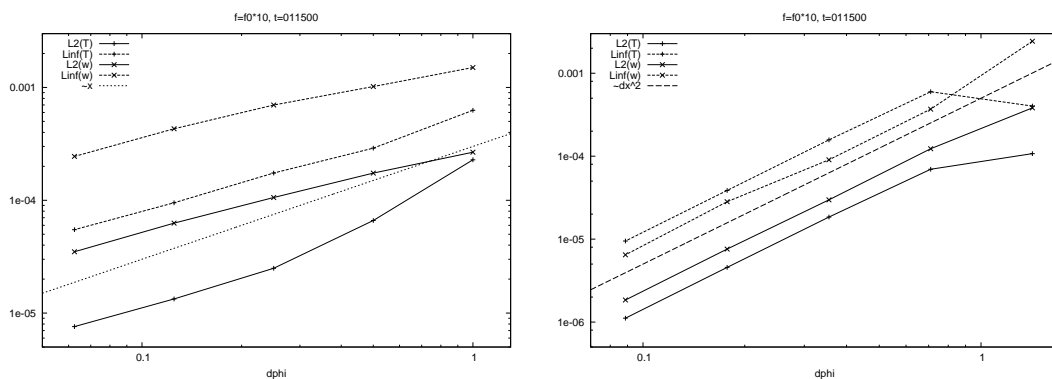

Figure 5: Error norms for 'test scenario B' with Coriolis force ('global f-plane approximation') with ICON. Left: use of slight vertical off-centring and time-level extrapolation in the pressure, right: without any off-centring

3 Influence of the water loading in strong convective simulations

At 20 June 2013, after a very hot period of 4 days in middle Europe, a front moved from Southwest during the evening. Whereas the front was simulated relatively well by the convection-permitting COSMO-DE, the precursory convergence line was much too weak and died out too early (figure 6, middle row) compared to the radar observations (figure 6, top row).

One reason for this behaviour was a bug in the water loading contribution of the buoyancy term in the equation for the vertical velocity. Since COSMO uses T' and p' as prognostic variables the buoyancy term must be rewritten with the aid of the ideal gas law by

$$-g\frac{\rho'}{\rho} = +g\left(\frac{p_0}{p}\frac{T'}{T_0} - \frac{p'}{p} + \frac{p_0}{p}\frac{T}{T_0}q_x\right) \tag{16}$$

with the moisture correction

$$q_x := \left(\frac{R_v}{R_d} - 1\right)q_v - q_c - q_r - \dots \tag{17}$$

in which q_v, q_c, and q_r are the specific masses of water vapour, cloud water, and rain, respectively.

In the previous versions the timelevel for these moisture variables was not the newest one ('now') but one time level older ('old'). The impact of this inconsistency is often small, however, in strongly convective situations it becomes crucial. This can be demonstrated by a simple idealised test setup. In a uniform grid with grid mesh size of $\Delta x = \Delta y = 2000$ m, $\Delta z = 400$ m a temperature perturbation of 2 K was set in *only one* grid box near the ground. The atmosphere is at rest and has a stable stratification analogous to those chosen in Weisman and Klemp (1982). Turbulent diffusion was switched off, only a 6-class Graupel microphysics scheme was used. This setup was tested with the 'now' and 'old' timelevel for the moisture variables in the water loading term. After the onset of condensation, the 'old' run always contains slightly more water vapour q_v and less condensate (q_c, q_r, ...) compared to the 'now' run. According to (17), both leads to stronger positive buoyancy and therefore to larger values of the maximum vertical velocity w_{max} (Figure 7, top left). After about half an hour, these differences in w_{max} reduce. Nevertheless, the production of cloud water q_c (Figure 7, top right) and consequently of rain q_r (bottom, left) is much larger in the 'now' run, leading to more precipitation at the ground (bottom, right).

Analogously the real case run with the 'now' timelevel for the 20 June 2013 produces more realistic precipitation rates (figure 6, bottom row). This example shows the importance of a proper treatment of the water loading contribution in the buoyancy term for strongly convective situations.

4 One-dimensional wave expansion with DG

In this section, we leave the 'Runge-Kutta' dynamical core of COSMO and will consider the Discontinuous Galerkin (DG) method, which is a relatively new approach in the meteorological modelling. DG methods are a combination of finite-element and finite-volume methods, i.e. the solutions are expanded into basis functions in each grid cell and the prognostic variables are conserved by using appropriate numerical flux formulations. An introduction into DG methods for conservation equations is given e.g. by Nair *et al.* (2011); see also the article by F. Giraldo in these proceedings.

Here, we want to highlight the wave expansion properties of a semi-discretisation by spatial DG methods for a simple example, the linear wave equation in one dimension

$$\frac{\partial u}{\partial t} + \frac{\partial f_u}{\partial x} = 0, \quad f_u := gh, \tag{18}$$

$$\frac{\partial h}{\partial t} + \frac{\partial f_h}{\partial x} = 0, \quad f_h := H_0 u. \tag{19}$$
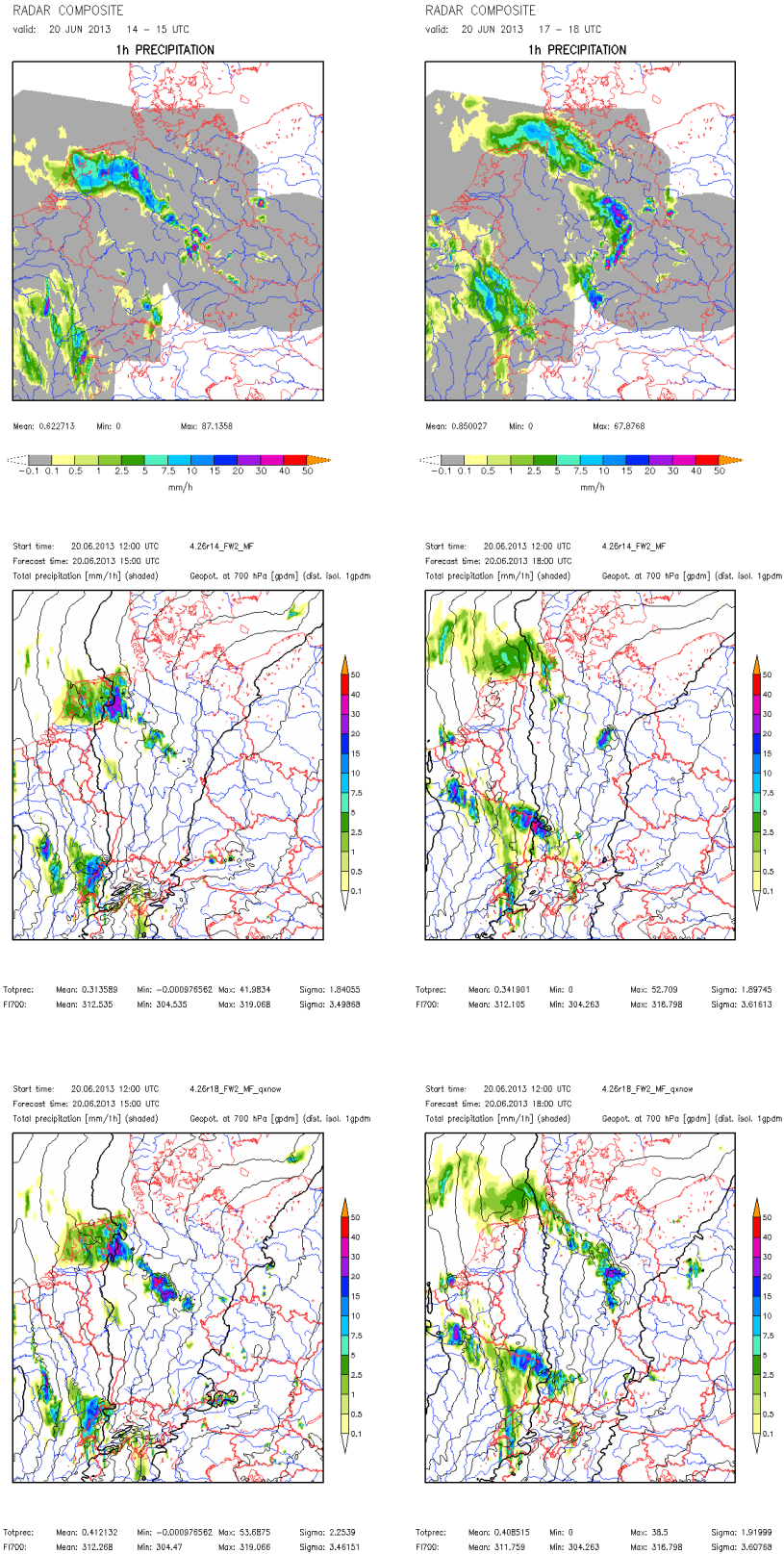
Figure 6: 1-hour precipitation sums for 20 June 2013. Top row: radar observations, middle row: COSMO-DE 12 UTC run with timelevel bug ('old'), bottom row: with correct timelevel ('now'). Left: at 15 UTC (after 3h simulation), right at 18 UTC (after 6 h).
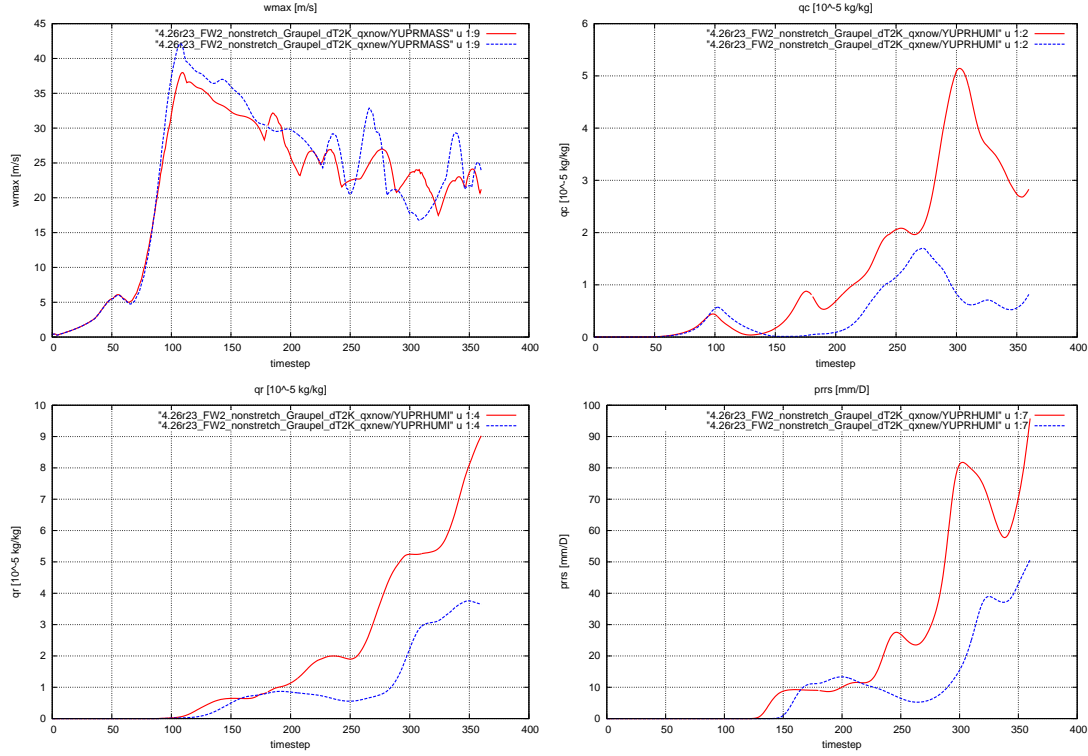
Figure 7: Time series of w_{max} and of averages of q_c, q_r and precipitation rate for the idealised convection test (timestep 20 sec.). Red lines: correct timelevel ('now'), blue: false timelevel ('old').

This can be considered as a simplified shallow water equation with constant gravity acceleration g and constant mean fluid depth H_0. Similar studies have been performed by Hu and Atkins (2002), who considered the 1D advection equation and the 2D wave equation, by Hu *et al.* (1999), who considered wave expansion through boundaries, and by Ainsworth (2004), who uses Bloch functions.

For the DG discretisation, we consider an equidistant grid with grid mesh size Δx. The j-th cell consists of the interval $\left[x_{j-\frac{1}{2}}, x_{j+\frac{1}{2}}\right]$ with the centre point x_j. In each grid cell j we expand the functions by Legendre-Polynomials P_l until polynomial degree p

$$u(x,t) = \sum_{l=0}^{p} \tilde{u}_{j,l}(t) \, P_l\left(2\frac{x-x_j}{\Delta x}\right), \tag{20}$$

$$h(x,t) = \sum_{l=0}^{p} \tilde{h}_{j,l}(t) \, P_l\left(2\frac{x-x_j}{\Delta x}\right). \tag{21}$$

The Legendre-Polynomials lead to the mass matrix

$$M_{j,lm} := \int_{x_{j-\frac{1}{2}}}^{x_{j+\frac{1}{2}}} P_l\left(2\frac{x-x_j}{\Delta x}\right) P_m\left(2\frac{x-x_j}{\Delta x}\right) dx = \delta_{lm} \frac{\Delta x}{2m+1}. \tag{22}$$

The DG formulation of the above wave equation system reads (for $m = 0, 1, \ldots, p$)

$$\frac{\Delta x}{2m+1}\frac{d}{dt}\tilde{u}_{j,m}(t) = -f_u^{num}(q(x-), q(x+)) P_m\left(2\frac{x-x_j}{\Delta x}\right)\Bigg|_{x_{j-\frac{1}{2}}+}^{x_{j+\frac{1}{2}}-}$$

$$+ \int_{I_j} f_u(q(x)) \cdot \frac{\partial P_m\left(2\frac{x-x_j}{\Delta x}\right)}{\partial x} \, dx, \tag{23}$$

$$\frac{\Delta x}{2m+1}\frac{d}{dt}\tilde{h}_{j,m}(t) = -f_h^{num}(q(x-),q(x+))\,P_m\left(2\frac{x-x_j}{\Delta x}\right)\Bigg|_{x_{j-\frac{1}{2}}+}^{x_{j+\frac{1}{2}}-}$$

$$+\int_{I_j} f_h(q(x))\cdot\frac{\partial P_m\left(2\frac{x-x_j}{\Delta x}\right)}{\partial x}\,dx. \tag{24}$$

Since the fluxes are linear functions with constant coefficients, we can calculate the flux integrals analytically. To this purpose, we define

$$B_{l,m} := \int_{x_{j-\frac{1}{2}}}^{x_{j+\frac{1}{2}}} P_l\left(2\frac{x-x_j}{\Delta x}\right)\frac{\partial P_m\left(2\frac{x-x_j}{\Delta x}\right)}{\partial x}\,dx. \tag{25}$$

One can show that for all $m \geq 0$, $l \geq 0$ these integrals are given by

$$B_{l,m} = \begin{cases} 0, & \text{if } m \leq l \text{ or } l+m \text{ is even} \\ 2, & \text{otherwise.} \end{cases} \tag{26}$$

One may argue, that in an actual numerical implementation, these integrals $B_{l,m}$ are calculated by quadrature formulae instead of an analytical integration. However, if one uses Gaussian quadrature (or, more precisely, Gauss-Legendre-quadrature), with p quadrature points, then the numerical quadrature is *exact* for polynomial degrees until $2p-1$, which is just the polynomial degree used for the $B_{l,m}$.

Now, we choose the *local Lax-Friedrichs-flux* for the numerical flux

$$f_u^{num}(q(x_{j+\frac{1}{2}}-),q(x_{j+\frac{1}{2}}+)) = \frac{1}{2}g\left(h(x_{j+\frac{1}{2}}+)+h(x_{j+\frac{1}{2}}-)\right)-\frac{1}{2}\alpha\left(u(x_{j+\frac{1}{2}}+)-u(x_{j+\frac{1}{2}}-)\right). \tag{27}$$

The numerical diffusion-parameter α is just the maximum eigenvalue of the Jacobian matrix $\mathbf{f}'(\mathbf{q})$. This is the characteristic velocity of the wave system

$$\alpha = c = \sqrt{gH_0}. \tag{28}$$

After insertion of the expansion (20) we get

$$f_u^{num}(q(x_{j+\frac{1}{2}}-),q(x_{j+\frac{1}{2}}+)) = \frac{1}{2}g\left(\sum_{l=0}^{p}\tilde{h}_{j+1,l}(t)\,(-1)^l+\sum_{l=0}^{p}\tilde{h}_{j,l}(t)\right)$$

$$-\frac{1}{2}\alpha\left(\sum_{l=0}^{p}\tilde{u}_{j+1,l}(t)\,(-1)^l-\sum_{l=0}^{p}\tilde{u}_{j,l}(t)\right) \tag{29}$$

and analogously

$$f_h^{num}(q(x_{j+\frac{1}{2}}-),q(x_{j+\frac{1}{2}}+)) = \frac{1}{2}H_0\left(\sum_{l=0}^{p}\tilde{u}_{j+1,l}(t)\,(-1)^l+\sum_{l=0}^{p}\tilde{u}_{j,l}(t)\right)$$

$$-\frac{1}{2}\alpha\left(\sum_{l=0}^{p}\tilde{h}_{j+1,l}(t)\,(-1)^l-\sum_{l=0}^{p}\tilde{h}_{j,l}(t)\right). \tag{30}$$

After some simplifications this leads to (for $m = 0,1,\ldots,p$):

$$\frac{\Delta x}{2m+1}\frac{d}{dt}\tilde{u}_{j,m}(t) = \frac{1}{2}g\sum_{l=0}^{p}\left[\tilde{h}_{j+1,l}(t)\,(-1)^{l+1}+\tilde{h}_{j,l}(t)\left(-1+(-1)^{l+m}+2B_{l,m}\right)+\tilde{h}_{j-1,l}(t)\,(-1)^m\right]$$

$$+\frac{1}{2}\alpha\sum_{l=0}^{p}\left[\tilde{u}_{j+1,l}(t)\,(-1)^l+\tilde{u}_{j,l}(t)\left(-1-(-1)^{l+m}\right)+\tilde{u}_{j-1,l}(t)\,(-1)^m\right], \tag{31}$$

$$\frac{\Delta x}{2m+1}\frac{d}{dt}\tilde{h}_{j,m}(t) = \frac{1}{2}H_0\sum_{l=0}^{p}\left[\tilde{u}_{j+1,l}(t)\,(-1)^{l+1}+\tilde{u}_{j,l}(t)\left(-1+(-1)^{l+m}+2B_{l,m}\right)+\tilde{u}_{j-1,l}(t)\,(-1)^m\right]$$

$$+\frac{1}{2}\alpha\sum_{l=0}^{p}\left[\tilde{h}_{j+1,l}(t)\,(-1)^l+\tilde{h}_{j,l}(t)\left(-1-(-1)^{l+m}\right)+\tilde{h}_{j-1,l}(t)\,(-1)^m\right]. \tag{32}$$

Of course, this leads to only 3-point operations, i.e. a DG method couples only neighbouring grid points.

4.1 The dispersion relation

We make a wave ansatz in the form

$$\tilde{u}_{j,m}(t) = \bar{u}_m(k,\omega)\, e^{i(kj\Delta x - \omega t)}, \tag{33}$$

$$\tilde{h}_{j,m}(t) = \bar{h}_m(k,\omega)\, e^{i(kj\Delta x - \omega t)}. \tag{34}$$

m distinguishes possible different *modes*. Here, a 'mode' is a continuous root of the dispersion relation (a slightly different meaning of 'modes' is used in the article of J. Thuburn in these proceedings). Inserted into in (31) and (32) results in

$$-i\omega \frac{\Delta x}{2m+1}\bar{u}_m = \frac{1}{2}g\sum_{l=0}^{p}\left[-e^{iK}\,(-1)^l + \left(-1+(-1)^{l+m}+2B_{l,m}\right)+e^{-iK}\,(-1)^m\right]\bar{h}_l$$

$$+ \frac{1}{2}\alpha\sum_{l=0}^{p}\left[e^{iK}\,(-1)^l + \left(-1-(-1)^{l+m}\right)+e^{-iK}\,(-1)^m\right]\bar{u}_l, \tag{35}$$

$$-i\omega \frac{\Delta x}{2m+1}\bar{h}_m = \frac{1}{2}H_0\sum_{l=0}^{p}\left[-e^{iK}\,(-1)^l + \left(-1+(-1)^{l+m}+2B_{l,m}\right)+e^{-iK}\,(-1)^m\right]\bar{u}_l$$

$$+ \frac{1}{2}\alpha\sum_{l=0}^{p}\left[e^{iK}\,(-1)^l + \left(-1-(-1)^{l+m}\right)+e^{-iK}\,(-1)^m\right]\bar{h}_l, \tag{36}$$

with the dimensionless wave number $K := k\Delta x$. This is a homogeneous linear equation system for the $2(p+1)$ variables $\bar{u}_l$ and $\bar{h}_l$. The dispersion relation $\omega(k)$ is determined by the polynomial $\det \mathbf{A} = 0$ of this linear equation system with the coefficient matrix $\mathbf{A}$.

In the following we use the dimensionless variables

$$\Omega := \omega\Delta t, \quad C := c\frac{\Delta t}{\Delta x}, \quad B := \frac{\alpha}{c}.$$

Consequently we can write the true dispersion relation $\omega = \pm ck$ as $\Omega = \pm CK$.

In the case $p = 0$, only constant functions are used as the basis. Therefore, this is just a normal finite-volume method. We get the dispersion relation

$$\Omega^2 + 2iBC(1-\cos K)\Omega + (B^2-1)C^2\sin^2 K - 2B^2C^2(1-\cos K) = 0, \tag{37}$$

which we can solve for Ω:

$$\Omega = \pm C\sin K - iBC(1-\cos K). \tag{38}$$

As expected, we get two branches (i.e. one mode for positive and negative expansion direction, respectively). The positive branch is plotted as the red line in both figures 10. One recognises that the real part of ω vanishes for $2\Delta x$-waves ($K = \pm\pi$). This is a general property and drawback of an A-grid (unstaggered grid) method. However, the internal numerical diffusion of the Lax-Friedrichs flux (and most other numerical flux formulations used) damps this short waves (negative value of the imaginary part of ω).

Next we consider the expansion into linear polynomials ($p = 1$). Now, the dispersion relation is

$$\Omega^4 + a_3\Omega^3 + a_2\Omega^2 + a_1\Omega^1 + a_0 = 0, \tag{39}$$

$$a_3 = 4iBC(\cos K + 2), \tag{40}$$

$$a_2 = 4(1-B^2)C^2\cos^2 K + (12-16B^2)C^2\cos K - 16(1+B^2)C^2, \tag{41}$$

$$a_1 = 24iBC^3(\cos K - 1), \tag{42}$$

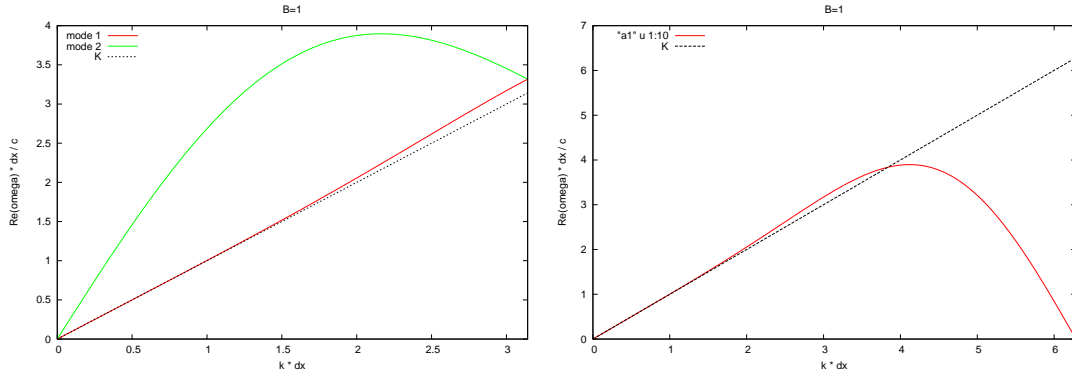$$a_0 = 36(B^2-1)C^4\sin^2 K + 72(1-\cos K)C^4. \tag{43}$$

Figure 8: Dispersion relation $Re\Omega(K)/C$ for $p = 1$ (only positive frequencies and for $k \geq 0$). Left: both modes ($0 \leq k\Delta x \leq \pi$), right: extended scheme ($0 \leq k\Delta x \leq 2\pi$).

We get 4 branches, i.e. two modes for the positive and two modes for the negative expansion direction. The two positive modes are shown on the left side in figure 8. Sometimes, the lower mode (which is quite close to the true dispersion relation $\Omega = CK$) is called the 'physical' mode, whereas the second mode is called 'spurious' or 'parasitic' mode. But if one mirrors this second mode to wave numbers in the range $\pi \leq K \leq 2\pi$, then one recognises, that this second mode also tries to approximate the true dispersion relation. Therefore, it is fair to denote it as a physical mode, too. Beyond, it is for each value α a *continuous* continuation of the first mode. However, the second mode turns against $\omega = 0$ now for the Δx-waves ($K = \pm 2\pi$). Again, we see that the DG discretisation indeed is an A-grid method. The good news is, that the numerical diffusion again damps these short waves, with a stronger scale selectivity compared to the above case $p = 0$.

Of course, the dispersion relation for quadratic base functions ($p = 2$) becomes even more complicated. Now, it consists of 6 branches (three modes for positive and negative expansion direction, respectively). Again, they approximate the true dispersion relation in a continuous manner, but only if the diffusion parameter α is larger than a certain value. As one recognises in figure 9, $\alpha/c > 0.15$ is necessary to get a continuous dispersion relation.

The above mentioned reflection of modes is used for figure 10 for the polynomial degrees $p = 0, 1, 2, 3$. For higher and higher degrees p, the dispersion relation better and better approximates the true dispersion relation. Of course, this results in increasing maximum values $\max|\omega|$ for the frequency. This naturally explains, why the Courant number limitation in DG methods decreases with increasing p. However, DG discretisations tend to overestimate the frequency to a certain extend. For $0 \leq p \leq 15$ an approximate relation of the form $\max|\omega|\Delta x/c \approx 1 + 2.6p + 0.33p^2$ was determined, i.e. the maximum frequency increases slightly stronger than linear with p. This indicates, that very high order DG methods with large p suffer too much from a Courant number limitation. Therefore, it is advisable not to choose too high order DG schemes.

In any case, for all polynomial degrees p the dispersion relation vanishes for the shortest waves with wave length $\lambda = 2/(p+1)\Delta x$ (or $K = \pm(p+1)\pi$). Therefore, DG methods are unstaggered grid discretisations. However, the numerical diffusion damps these shortest waves and the increasing scale selectivity in the damping of short waves, indicated by the imaginary part of ω in 10 (right), is an argument to use not too small values for p.
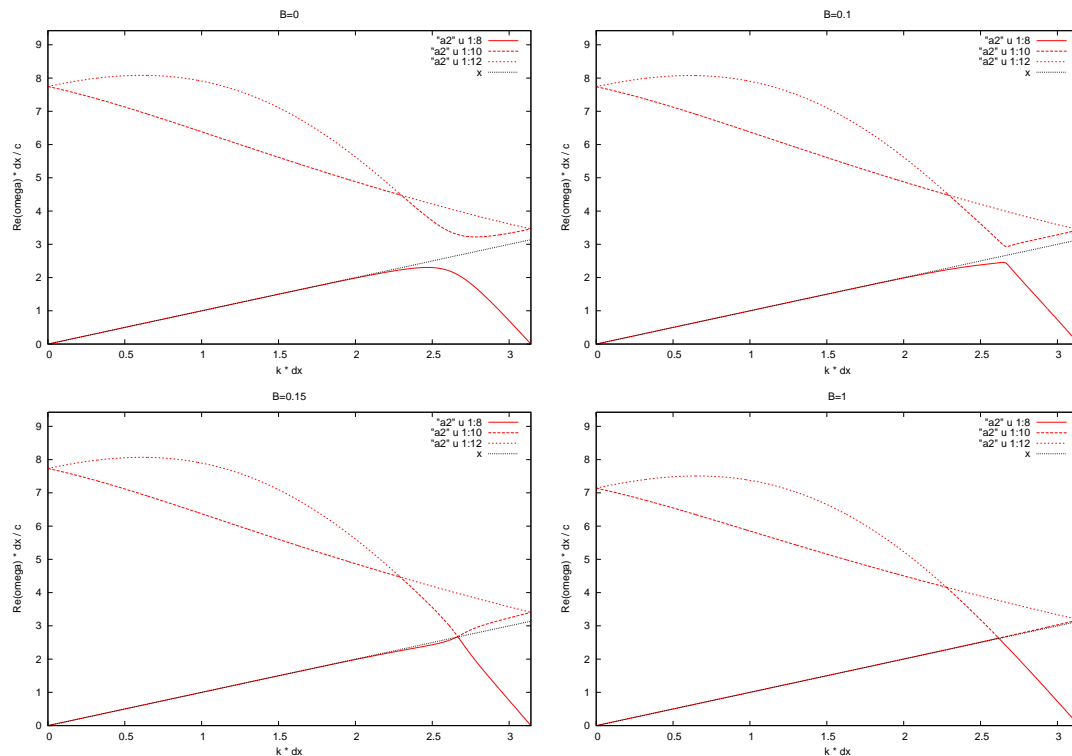
Figure 9: Dispersion relation $Re\,\Omega(K)/C$ of DG for polynomial degree $p = 2$ and different numerical diffusion parameter values $B = 0, 0.1, 0.15, 1$.

References

Ainsworth M. 2004. Dispersive and dissipative behaviour of high order discontinuous Galerkin finite element methods. *J. Comput. Phys.* **198**: 106–130.

Baldauf M. 2008. Stability analysis for linear discretisations of the advection equation with Runge-Kutta time integration. *J. Comput. Phys.* **227**: 6638–6659.

Baldauf M. 2010. Linear stability analysis of Runge-Kutta based partial time-splitting schemes for the Euler equations. *Mon. Weather Rev.* **138**: 4475–4496.

Baldauf M. 2013. A new fast-waves solver for the Runge-Kutta dynamical core. Technical Report 21, Consortium for Small-Scale Modelling, www.cosmo-model.org.

Baldauf M, Brdar S. 2013. An analytic solution for linear gravity waves in a channel as a test for numerical models using the non-hydrostatic, compressible Euler equations. *Quart. J. Royal Meteorol. Soc.* (DOI:10.1002/qj.2105).

Baldauf M, Fuhrer O, Kurowski MJ, de Morsier G, Müllner M, Piotrowski ZP, Rosa B, Vitagliano PL, Wójcik D, Ziemiański M. 2013a. The COSMO Priority Project 'Conservative Dynamical Core' - Final Report. Technical Report 23, COSMO-Consortium.

Baldauf M, Reinert D, Zängl G. 2013b. An analytical solution for linear gravity and sound waves on the sphere as a test for compressible, non-hydrostatic numerical models. *Quart. J. Royal Meteorol. Soc.* (accepted with minor revisions).
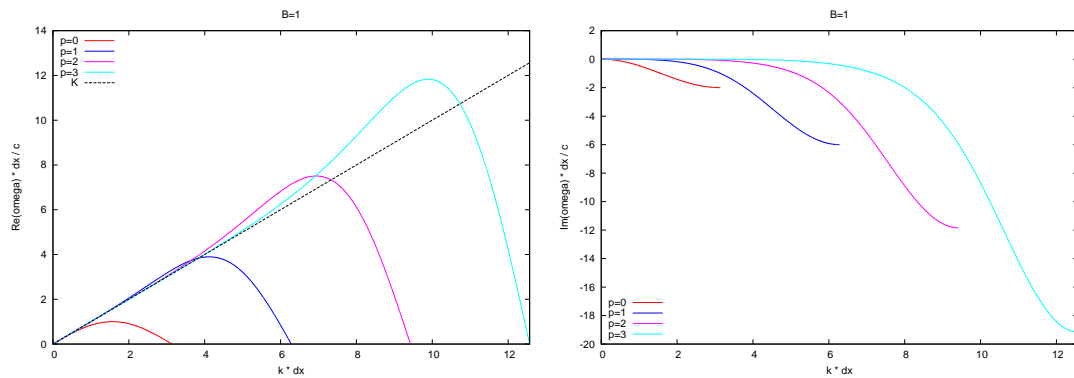
Figure 10: Dispersion relation $\Omega(K)/C$ of DG for different polynomial degrees $p = 0, 1, 2, 3$. Left: real part of Ω, right: imaginary part of Ω.

Hu FQ, Atkins HL. 2002. Eigensolution Analysis of the Discontinuous Galerkin Method with Nonuniform Grids. *J. Comput. Phys.* **182**: 516–545.

Hu FQ, Hussaini MY, Rasetarinera P. 1999. An Analysis of the Discontinuous Galerkin Method for Wave Propagation Problems. *J. Comput. Phys.* **151**: 921–946.

Ikeda T, Durbin PA. 2004. Mesh stretch effects on convection in flow simulations. *J. Comput. Phys.* **199**: 110–125.

Jameson A. 1991. Time Dependent Calculations Using Multigrid, with Applications to Unsteady Flows Past Airfoils and Wings. In: *AIAA 10th Computational Fluid Dynamics Conference*. pp. 1–13.

Mahrer Y. 1984. An Improved Numerical Approximation of the Horizontal Gradients in a Terrain-Following Coordinate System. *Mon. Weather Rev.* **112**: 918–922.

Nair RD, Levy MN, Lauritzen PH. 2011. Emerging Numerical Methods for Atmospheric Modeling. In: *Numerical Techniques for Global Atmospheric Models*, Lauritzen PH, Jablonowski C, Taylor MA, Nair RD (eds), Springer, p. 564p.

Prusa JM, Smolarkiewicz PK, Wyszogrodzki AA. 2008. EULAG, a computational model for multiscale flows. *Computers and Fluids* **37**(9): 1193–1207.

Skamarock WC, Klemp JB. 1994. Efficiency and accuracy of the Klemp-Wilhelmson Time-Splitting scheme. *Mon. Weather Rev.* **122**: 2623–2630.

Weisman ML, Klemp JB. 1982. The dependence of Numerically Simulated Convective Storms on Vertical Wind Shear and Buoyancy. *Mon. Weather Rev.* **110**: 504–520.

Wicker LJ, Skamarock WC. 2002. Time Splitting Methods for Elastic Models using Forward Time Schemes. *Mon. Weather Rev.* **130**: 2088–2097.